

The impact of strong gravitational lensing on observed Lyman-break galaxy numbers at $4 \leq z \leq 8$ in the GOODS and the XDF blank fields

R. L. Barone-Nugent,^{1★} J. S. B. Wyithe,¹ M. Trenti,^{1,2} T. Treu,³ P. Oesch,⁴
R. Bouwens,⁵ G. D. Illingworth⁶ and K. B. Schmidt³

¹*School of Physics, University of Melbourne, Parkville, VIC 3010, Australia*

²*Kavli Institute for Cosmology and Institute of Astronomy, University of Cambridge, Cambridge CB2 1TN, UK*

³*Department of Physics, University of California, Santa Barbara, CA 93106-9530, USA*

⁴*Department of Astronomy, Yale University, New Haven, CT 06511, USA*

⁵*Leiden Observatory, Leiden University, NL-2300 RA Leiden, the Netherlands*

⁶*UCO/Lick Observatory, University of California, Santa Cruz, CA 95064, USA*

Accepted 2015 March 23. Received 2015 March 3; in original form 2014 December 18

ABSTRACT

Detections of Lyman-break galaxies (LBGs) at high-redshift are affected by gravitational lensing induced by foreground deflectors not only in galaxy clusters, but also in blank fields. We quantify the impact of strong magnification in the samples of B_{435} , V_{606} , i_{775} and z_{850} & Y_{105} dropouts ($4 \lesssim z \lesssim 8$) observed in the eXtreme Deep Field (XDF) and the Cosmic Assembly Near-infrared Deep Extragalactic Legacy Survey (CANDELS) fields by investigating the proximity of dropouts to foreground objects. We find that ~ 6 per cent of bright $z \sim 7$ LBGs ($m_{H_{160}} < 26$) have been strongly lensed ($\mu > 2$) by foreground objects. This fraction decreases from ~ 3.5 per cent at $z \sim 6$ to ~ 1.5 per cent at $z \sim 4$. Since the observed fraction of strongly lensed LBGs is a function of the shape of the luminosity function (LF), it can be used to derive Schechter parameters, α and M_* , independently from galaxy number counts. Our magnification bias analysis yields Schechter-function parameters in close agreement with those determined from galaxy counts albeit with larger uncertainties. Extrapolation of our analysis to $z \gtrsim 8$ suggests that surveys with *JWST*, *WFIRST* and *Euclid* should find excess LBGs at the bright end, over an intrinsic exponential cutoff. Finally, we highlight how the magnification bias measurement near the XDF detection limit can be used to probe the population of galaxies beyond this limit. Preliminary results suggest that the magnification bias at $M_{UV} \sim -18$ is weaker than expected if $\alpha \lesssim -1.7$ extends well below the current detection limits. This could imply a flattening of the LF at $M_{UV} \gtrsim -16.5$. However, selection effects and completeness estimates are difficult to quantify precisely. Thus, we do not rule out a steep LF extending to $M_{UV} \gtrsim -15$.

Key words: gravitational lensing: strong – galaxies: high-redshift – galaxies: luminosity function, mass function – cosmology: observations.

1 INTRODUCTION

Surveys of Lyman-break galaxies (LBGs) during the epoch of reionization aim to make a census of high-redshift galaxies and to estimate the available ionizing photon budget for reionization (Khochfar et al. 2007; Bouwens et al. 2008, 2011, 2014; Castellano et al. 2010; Bradley et al. 2012; Finkelstein et al. 2012, 2014; Oesch et al. 2012; McLure et al. 2013; Robertson et al. 2013; Schenker et al. 2013; Schmidt et al. 2014). These surveys, however,

may provide an increasingly skewed view of the early Universe as redshift increases. The observations are complicated by gravitational lensing (Wyithe et al. 2011), which affects the observed luminosities and surface density of high-redshift LBGs. Along random lines of sight, the probability of significant magnification and multiple images from gravitational lensing is ~ 0.5 per cent (Barkana & Loeb 2000; Comerford, Haiman & Schaye 2002; Wyithe et al. 2011). Furthermore, high-redshift luminosity functions (LFs) have been shown to have very steep faint-end slopes ($\alpha \sim -1.6$ at $z \sim 4$ to $\alpha \sim -2.0$ at $z \sim 8$, although the uncertainties are large, e.g. Bouwens et al. 2014; Schmidt et al. 2014), which results in a bias leading to an enhanced probability of gravitational lensing over

* E-mail: robertbn@student.unimelb.edu.au

random lines of sight. This so-called *magnification bias* is further enhanced for flux limits at magnitudes brighter than M_* where number counts drop exponentially. Consequently, bright LBGs become much more likely to have been gravitationally lensed than random lines of sight (Wyithe et al. 2011). The strongly lensed fraction of LBGs at $z \sim 7$ –8 brighter than M_* is expected to be ~ 10 per cent.

The amplitude of magnification bias is a function of $M_* - M_{\text{lim}}$ and α (Pei 1995; Wyithe et al. 2011), where M_{lim} is the survey flux limit. Therefore, quantifying the amount of magnification bias offers a direct probe of the LF down to, and below, current survey detection limits (Mashian & Loeb 2013). Alternative approaches to quantifying the LF beyond detection limits exist, such as targeting massive galaxy clusters as gravitational lenses (Alavi et al. 2014; Yue et al. 2014; Atek et al. 2015; Ishigaki et al. 2015) and assessing the noise characteristics of the background (Calvi et al. 2013).

Magnification bias is expected to significantly skew the observed bright end of the LF at very high redshifts (see fig. 3 in Wyithe et al. 2011). The effect is intriguing in light of the $z \sim 7$ LF, which has been observed to both agree with the exponential cutoff in the Schechter parametrization (Bouwens et al. 2014), and also to decline less steeply than a Schechter function (Bowler et al. 2014). Previous studies of high-redshift galaxies have argued that gravitational lensing has not significantly affected their LFs (McLure et al. 2006), while others have made slight corrections in the observed luminosities of LBGs due to gravitational lensing (Bowler et al. 2014). However, even though the sample sizes analysed in recent studies are large, the numbers of bright galaxies, where the magnification bias effects will be most apparent, remain small. Thus observational verification of any changes to the slope at the bright end remains to be determined.

Identifying and confirming individual cases of strong gravitational lensing of LBGs at $z \gtrsim 4$ is made difficult due to sources appearing faint and small. Elongation in the observed LBG due to lensing is difficult to detect due to their small observed size compared with the resolution of the telescope. Secondary images are very difficult to observe, as they will be less magnified than the primary image, and hence be extremely faint (Barone-Nugent et al. 2013). Secondary images will also appear closer to the deflector than the primary image, making it more difficult to disentangle them from the deflector galaxy light than the primary image. Wyithe et al. (2011) calculated the probability of detecting a secondary image to be ≈ 10 per cent, where the bright image of a galaxy is 1 mag above the survey limit.

In this paper, we adopt a statistical approach to detect gravitational lensing of high-redshift galaxies using the largest samples of LBGs at $4 \leq z \leq 8$ (Bouwens et al. 2014). We assess the likelihood of lensing for each individual LBG in homogenous samples at $z \sim 4$, $z \sim 5$, $z \sim 6$ and $z \sim 7$ –8 in order to infer the total expected lensed fraction at a range of flux limits. In Section 2, we describe the data used in our analysis. In Section 3, we derive the Faber–Jackson relation (FJR; Faber & Jackson 1976) of foreground galaxies that we will use in our analysis. Section 4 describes our method of prescribing a likelihood of lensing to each LBG. Section 5 describes our lensing results and in Section 6, we assess the magnification bias and the consequences for the LF beyond current survey limits. In Section 7, we assess the observational effects of magnification bias on the LF and in Section 8, we present the strong lensing likelihoods of existing $z \sim 9$ –10 LBGs. In Section 9, we conclude. We refer to the *HST* $F435W$, $F606W$, $F775W$, $F850LP$, $F105W$, $F125W$ and $F160W$ bands as B_{435} , V_{606} , i_{775} , z_{850} , Y_{105} , J_{125} and H_{160} . Throughout this paper, we use $\Omega_M = 0.3$, $\Omega_\Lambda = 0.7$ and

$H_0 = 70 \text{ km s}^{-1} \text{ Mpc}^{-1}$, and all magnitudes are in the AB system (Oke & Gunn 1983).

2 DATA

The analysis presented in this paper makes use of the wide-area, ultra-deep observations of the XDF/UDF and GOODS (from the XDF, ERS and CANDELS programmes) (Grogin et al. 2011; Koekemoer et al. 2011; Windhorst et al. 2011; Illingworth et al. 2013). The observations cover the 4.7 arcmin² area of the XDF, which reaches ~ 30 mag at 5σ , the 126 arcmin² of the GOODS Deep fields, which reach ~ 28.5 mag at 5σ , and the 115 arcmin² of the GOODS wide fields, which reach ~ 27.7 mag at 5σ . The catalogues were constructed to identify LBGs from $z \sim 4$ to $z \sim 8$ using a colour–colour criteria (see the details in section 3.2.2 of Bouwens et al. 2014). LBGs ‘drop out’ in the B_{435} , V_{606} , i_{775} , z_{850} and Y_{105} for LBGs at $z \sim 4$, $z \sim 5$, $z \sim 6$, $z \sim 7$ and $z \sim 8$, respectively. The catalogues include 5867, 2108, 691, 455 and 155 LBG candidates at $z \sim 4$, $z \sim 5$, $z \sim 6$, $z \sim 7$ and $z \sim 8$, respectively.

We use the 3D-HST photometric catalogue of the CANDELS area (Brammer et al. 2012; Skelton et al. 2014) in order to model foreground objects as potential gravitational lenses. The 3D-HST survey covers all of the CANDELS fields, with spectroscopy compiled from the literature. We utilize the spectroscopic redshifts of foreground objects when available, and otherwise rely on photometric redshifts obtained using *EAZY* (Brammer, van Dokkum & Coppi 2008) which are based on deep multiband observations (Taniguchi et al. 2007; Barmby et al. 2008; Erben et al. 2009; Grogin et al. 2011; Koekemoer et al. 2011; Whitaker et al. 2011; Bielby et al. 2012; Brammer et al. 2012; McCracken et al. 2012; Ashby et al. 2013).

We calibrate a redshift-dependent Faber–Jackson relation (Faber & Jackson 1976) in Section 3 using early-type galaxy data from Treu et al. (2005), Auger et al. (2009) and Newman et al. (2010). The galaxies in these samples have published spectroscopic redshifts, velocity dispersions and rest-frame B -band magnitudes.

3 THE FABER–JACKSON RELATION

There exists a spatial correlation between bright, high- z LBGs and bright foreground objects (see Appendix A). Spatial correlations between source LBGs and foreground objects suggests that magnification bias is detectable in current surveys. In order to quantify its extent, foreground objects need to be modelled as gravitational lenses.

The key parameter determining the efficiency of an early-type galaxy as a gravitational lens is its velocity dispersion (Turner, Ostriker & Gott 1984). We estimate the velocity dispersion of each galaxy in the CANDELS field from its photometry by calibrating a redshift-dependent Faber–Jackson relation (FJR; Faber & Jackson 1976). The FJR relates the luminosity of an object to its velocity dispersion. We include a redshift evolution term to account for the evolution of the mass-to-light ratio with increasing redshift, so the FJR can be expressed as

$$L_B = m\sigma_*^\gamma(1+z)^\beta, \quad (1)$$

where L_B is the B -band luminosity, σ_* is the stellar velocity dispersion and z is the redshift. The FJR can be expressed linearly as

$$M_B = ax + by + c, \quad (2)$$

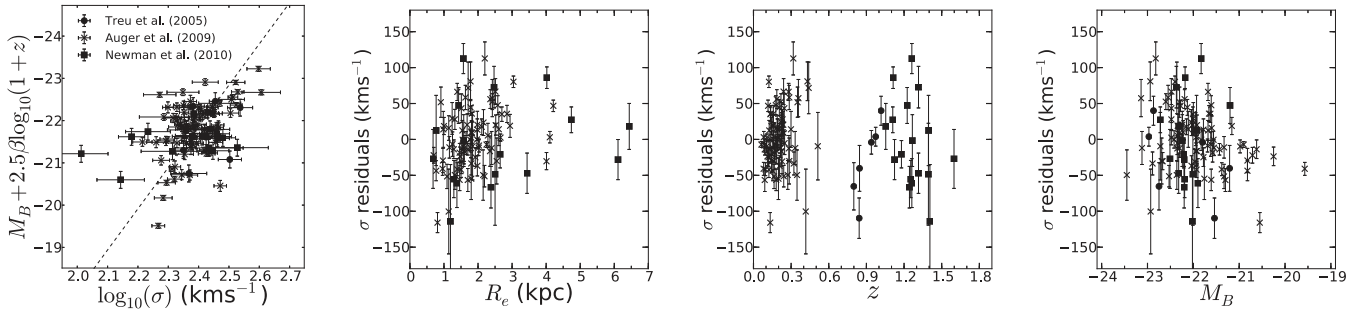


Figure 1. Left: the FJR that we derive (dashed) projected along the z -axis and the galaxies in the three samples of Treu et al. (2005), Auger et al. (2009) and Newman et al. (2010). We find no systematic biases in the FJR we derive. Centre left: the residuals of the velocity dispersions of the galaxies in the Auger et al. (2009) and Newman et al. (2010) samples as a function of effective radius. Centre right: the residuals of the velocity dispersions of the galaxies in the three samples as a function of redshift. The scatter in the residuals at $z > 0.6$ agrees with the scatter in the residuals at $z < 0.6$ within the uncertainties. Right: the residuals of the velocity dispersions as a function of the B -band magnitude.

where $a = -2.5\gamma$, $x = \log_{10} \frac{\sigma_*}{200 \text{ km s}^{-1}}$, $b = -2.5\beta$, $y = \log_{10}(1+z)$, $c = -2.5 \log_{10}(m)$ and $M_B = -2.5 \log_{10}(L_B)$. We calibrate the FJR using galaxies with spectroscopic redshifts and velocity dispersions from Treu et al. (2005), Auger et al. (2009) and Newman et al. (2010), which span $0 < z < 1.6$. We determine the values of a , b and c by minimizing the χ^2 , given by

$$\chi^2 = \sum_{i=0}^n \frac{(M_{B_i} - ax_i - by_i - c)^2}{(\epsilon_{M_{B_i}}^2 + a^2 \epsilon_{x_i}^2 + b^2 \epsilon_{y_i}^2 + \epsilon_{\text{int}}^2)}, \quad (3)$$

where $\epsilon_{M_B, x, y}$ are the uncertainties in the data and ϵ_{int} is the intrinsic scatter. To avoid degeneracies, we fix the slope to be $\gamma = 3.9$, in line with previous studies (Hyde & Bernardi 2009a; Jönsson et al. 2010).

We find best-fitting parameters of $m = 2.3 \pm 0.2 \times 10^8$ and $\beta = 0.7 \pm 0.3$. The errors on m and β are not independent, so the uncertainty in the inferred velocity dispersion due to their uncertainty is $\sim 10 \text{ km s}^{-1}$, and will not significantly affect the inferred strongly lensed fraction. The FJR is plotted in the left-hand panel of Fig. 1, and the residuals are plotted as a function of effective radius, R_e , redshift, z , and B -band magnitude, M_B are plotted in the centre-left, centre-right and right-hand panels, respectively. The uncertainty in the FJR is dominated by the intrinsic scatter, which is 46 km s^{-1} in the direction of velocity dispersion. There are no systematic biases in the residuals with respect to M_B , z or the R_e . The scatter in the residuals for galaxies at $z > 0.6$ is consistent with galaxies at $z < 0.6$, with no evidence of redshift-dependent scatter in our FJR.

The resultant FJR is consistent with B -band FJRs found from weak lensing analyses of Type Ia supernovae presented by Jönsson et al. (2010), Kleinheinrich et al. (2006) and Hoekstra, Yee & Gladders (2004). As a check of our FJR, we compare it with the i^* -band FJR (which may be less prone to dust-extinction) presented by Bernardi et al. (2003) for all objects in GOODS. We find very close agreement between σ_* as inferred from the i^* -band FJR with our B -band FJR. For low-redshift objects, the scatter in the residuals between the two methods is 2 km s^{-1} . For all objects out to $z = 2$, the scatter in the residuals between the two FJRs is 9 km s^{-1} . This may be partially due to the Bernardi et al. (2003) FJR being calibrated at $z \sim 0$, and not taking into account redshift evolution. There are no systematic biases in the residuals between these two FJRs as a function of z , M_B or R_e .

We compare our FJR with estimates of velocity dispersions using the stellar mass estimates of galaxies in our calibration sample using the relation between stellar mass and velocity dispersion presented

by Hyde & Bernardi (2009b). We find the scatter in the residuals of velocity dispersion estimates using this method to be very similar (in fact, slightly larger) than those found using our FJR. This suggests that using stellar mass information rather than L_B will not significantly reduce the scatter in our velocity dispersion estimates.

4 ASSESSING THE STRONG LENSING LIKELIHOOD OF LBGs

To quantify the strongly lensed fraction of LBGs, we model every foreground object in the field as a gravitational lens. Using photometric information of all foreground objects, we ask the following question for each LBG: What is the likelihood of this LBG being gravitationally lensed with magnification $\mu > 2$ given its position relative to nearby (in projection) foreground objects? We disregard deflector–LBG pairs with a separation of $\theta_{\text{sep}} > 5.0$ arcsec, which is much larger than the Einstein radius of typical deflectors. While the choice of maximum separation of 5.0 arcsec is somewhat arbitrary, we show in Section 5.2 that 5.0 arcsec is a reasonable choice. For each foreground object within 5.0 arcsec of the LBG, we use the following process.

- (i) Model the foreground object using a singular isothermal sphere (SIS) density profile.
- (ii) Calculate the velocity dispersion that the foreground object requires for it to produce an image at the observed position of the LBG with a magnification of $\mu = 2$, denoted by $\sigma_{*, \text{req}}$. For an SIS, $\mu = 2$ marks the beginning of the strong lensing regime. The required velocity dispersion depends on the LBG–deflector separation, LBG redshift and deflector redshift.
- (iii) Calculate the likelihood that the foreground object has a velocity dispersion greater than or equal to $\sigma_{*, \text{req}}$. This is the likelihood of strong lensing for that deflector–LBG pair.
- (iv) Weight the likelihood of lensing by the inverse of the detection completeness at the separation between the LBG and the nearby foreground object.

The final step accounts for reduced sensitivity to faint LBGs nearby bright foregrounds. We explain this process further in Section 4.1.

To calculate $\sigma_{*, \text{req}}$ we find the Einstein radius, θ_{ER} , required for $\mu = 2$ using the expression for the magnification of the image in an observed configuration

$$\mu = \frac{|\theta_{\text{sep}}|}{|\theta_{\text{sep}}| - \theta_{\text{ER}}}, \quad (4)$$

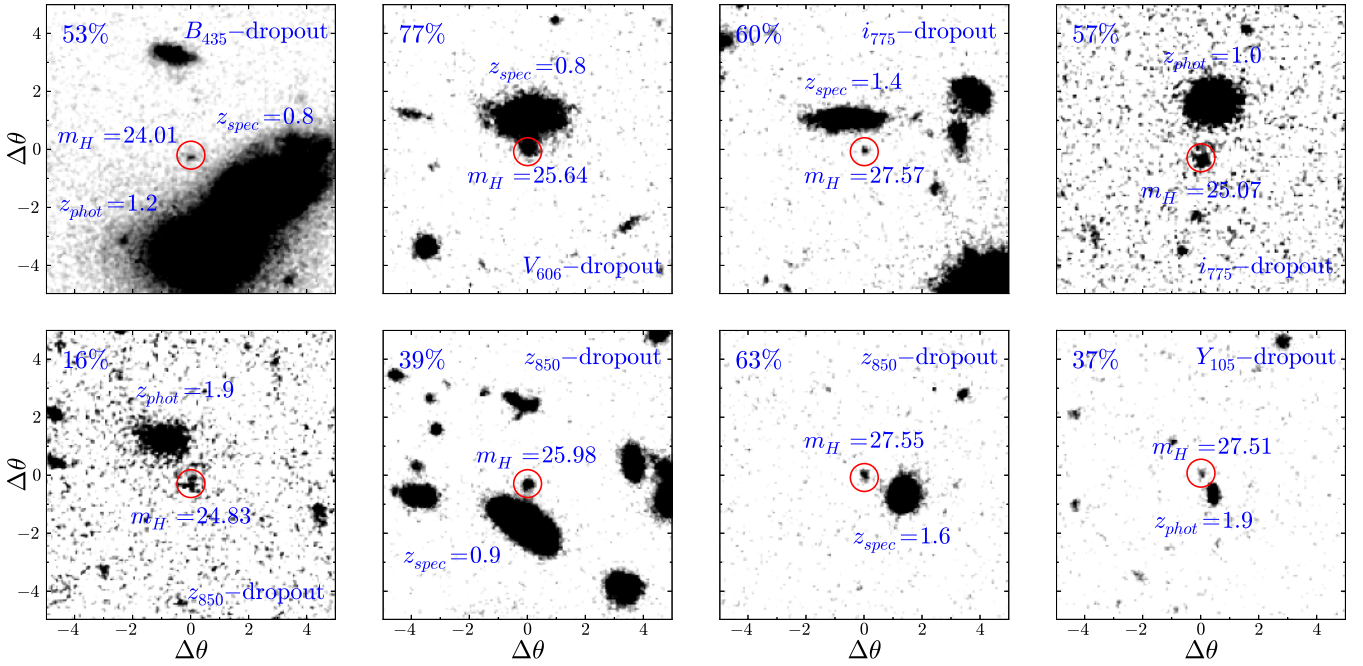


Figure 2. Examples of possibly lensed LBGs in the four samples. All cutouts are of the J_{125} images, are 10.0×10.0 arcsec and are shown on the same contrast scale (except for the top-left cutout, which contains two very bright foreground galaxies). The LBGs are circled in red and the deflectors are labelled by their spectroscopic/photometric redshifts. Each LBG is labelled with its H_{160} magnitude, and its likelihood of being strongly lensed (top-left corner). The LBG shown in the bottom-left panel is the brightest LBG in the $z \sim 7$ sample.

where μ is the magnification, and θ_{sep} is the observed separation between the source image and the deflector. We can then find the velocity dispersion corresponding to $\mu = 2$ using the expression for the Einstein radius of an SIS

$$\theta_{\text{ER}} = 4\pi \left(\frac{\sigma_*}{c} \right)^2 \frac{D_{\text{LS}}}{D_S}, \quad (5)$$

where σ_* is the stellar velocity dispersion, D_S is the angular diameter distance to the source and D_{LS} is the angular diameter distance from the lens to the source.

For each LBG–foreground object pair, the likelihood of strong lensing of the LBG by the deflector is equal to the likelihood that the deflector has a velocity dispersion above $\sigma_{*,\text{req}}$, which is given by

$$\mathcal{L} = \frac{1}{2} \text{erfc} \left(\frac{\sigma_{*,\text{req}} - \sigma_{*,\text{inf}}}{\sqrt{2}\epsilon_{\text{FJR}}} \right), \quad (6)$$

where $\sigma_{*,\text{inf}}$ is the velocity dispersion inferred from photometry (using the FJR), and ϵ_{FJR} is the intrinsic scatter in the velocity dispersion of the FJR.

In the event that there are multiple potential deflectors within 5.0 arcsec of the source, we treat them independently and calculate the probability that at least one is lensing the source by $\mu \geq 2$. For n deflectors, this is

$$\mathcal{L} = 1 - \prod_{j=1}^n (1 - \mathcal{L}_j). \quad (7)$$

We show a subset of the sample consisting of some of the highest-likelihood lenses in Fig. 2. We describe these systems further in Section 5.1.

4.1 Accounting for sensitivity variations

Faint LBG samples have a reduced completeness compared to bright ones. This alone would not affect our inference of the lensed fraction, because the completeness would change the numerator and the denominator by the same factor at fixed magnitude. However, we note that there may be a further reduced sensitivity to detecting faint LBGs around bright objects, which will affect potentially lensed LBGs differently to those isolated in the field. This effect could cause our measured strongly lensed fraction to be artificially low.

We weight all LBGs that appear close in projection to bright foreground objects by the inverse of their relative detection probability in order to account for reduced sensitivity around foreground objects. To do this, we run completeness simulations around all foreground objects which are either

- (i) assessed as having a greater than 1 per cent chance of lensing a nearby LBG, or,
- (ii) brighter than $m_r = 24$ mag and within 2.5 arcsec of an LBG.

We run source recovery simulations in order to determine completeness as a function of radius around each foreground meeting either of the above criteria. The source recovery simulations are run for LBGs¹ at the redshift and of the magnitude corresponding to that of the nearby LBG. The completeness of a source LBG, s_c , becomes unaffected by typical foregrounds at a separation of around 1.5–2.0 arcsec. The weight, w_c , we apply to each LBG is defined as

¹ The artificial sources in the recovery simulations are extended, and have sizes typical of LBGs at the appropriate redshift. It should be noted that strong lensing may cause the sources to appear more extended, which will affect their completeness. This effect is expected to be small, but is a slight limitation of this analysis.

the inverse of the completeness, $w_c \equiv 1/s_c$. We apply a maximum weighting of $w_c = 10$ to any LBG.

We find that weighting the lensed fraction in this way has a minimal effect on the bright end of the observed lensed fraction. However, the relative completeness of faint galaxies near to bright foreground galaxies is, as expected, lower than for the brighter LBGs.

4.2 Uncertainty checks

The typical uncertainty in the photometric redshifts of foreground sources derived in the 3D-HST catalogues are $\Delta z \sim 0.1$ – 0.2 , so the uncertainty in the magnification is dominated by the intrinsic uncertainty in the FJR. Furthermore, the uncertainty in M_B due to photometric redshift errors (via the distance modulus) is partially self-regulating as the inferred velocity dispersion is a decaying function of redshift, while inferred rest-frame luminosity is an increasing function. We find that of the 40 $z \sim 7$ LBGs that have a likelihood of lensing of ≥ 10 per cent, the deflector of only one has a photometric redshift with less than an 80 per cent chance of residing within $\Delta z = 0.2$. None of the deflectors of $z \sim 4$ – 6 LBGs with a likelihood of lensing of ≥ 10 per cent have photometric redshifts with less than an 80 per cent chance of residing within $\Delta z = 0.2$. The uncertainty in source redshift ($\Delta z \sim 0.35$) is negligible as the angular diameter distance is a relatively flat function at high redshift.

There is a possible Eddington bias stemming from uncertainties in the photometry and the shape of the LF at $z \sim 1$, which could bias the inference of σ_* from the B -band luminosity. We find that $\Psi(L \pm \delta L)$ only varies by 2–5 per cent from $\Psi(L)$ for galaxies brighter than $\sim M_*$ at $z = 1$ in the field. Therefore, the number density of bright galaxies does not change significantly within the photometric uncertainties, and the Eddington bias is negligible.

We note that a limitation of this analysis is that it assumes all deflectors to be SISs. Singular isothermal ellipsoids (SIEs) may be a more realistic parametrization of potential deflectors (see Keeton 2001, for ellipsoidal density parametrizations). However, SIEs do complicate the calculation significantly (Kormann, Schneider & Bartelmann 1994; Huterer, Keeton & Ma 2005). The median ellipticity for all objects in the CANDELS fields is $\bar{\epsilon} = 0.21$, with 83 per cent having an ellipticity of $\epsilon < 0.4$. In the case of low deflector ellipticity ($\epsilon \lesssim 0.2$), the change in the magnification estimate is ≈ 10 per cent along both the major (+10 per cent) and minor (–10 per cent) axes. For larger ellipticities ($\epsilon \approx 0.4$), the magnification estimate becomes ≈ 20 per cent lower for an image located along the minor axis, and a factor of 2 higher for images along the major axis. Using an elliptical deflector model for the system shown in the bottom, centre-left panel of Fig. 2, which includes a deflector with large ellipticity ($\epsilon = 0.48$), we estimate the magnification to be $\mu \simeq 1.6$, as compared with the SIS estimation of $\mu \simeq 1.8$. The LBG in the bottom-right panel of Fig. 2, which is near a deflector with ellipticity $\epsilon = 0.33$, has a magnification of $\mu \simeq 1.6$ in the SIS model, which becomes $\mu \simeq 1.9$ using an ellipsoidal model.

Similarly, the lensing cross-section (the strong lensing area in the image plane owing to a deflector) of an SIE is the same as the optical depth of an SIS with a higher order term (Kormann et al. 1994). The area of sky covered by the Einstein radius of an SIE is only ≈ 5 per cent larger than the area of sky covered by an SIS for reasonable ellipticities ($\epsilon \lesssim 0.4$). Therefore, our calculations of the optical depth in Section 6 are not significantly affected by the SIS assumption. These calculations are consistent with previous studies of the effect of ellipticity on the strong lensing optical depth and magnification, such as Huterer et al. (2005) who

noted that aside from image multiplicities, introducing shear and ellipticity has surprisingly little effect. Hence, using an SIE deflector will not qualitatively change either our strongly lensed fraction or magnification bias results.

5 THE STRONGLY LENSED FRACTION

The method of prescribing a likelihood of strong lensing described in Section 4 was applied to each LBG in the samples at $z \sim 4$, $z \sim 5$, $z \sim 6$ and $z \sim 7$ – 8 . The 455 z_{850} dropouts and 155 Y_{105} dropouts were combined to create a statistically significant sample with a mean redshift of $\bar{z} = 7.2$. The number of strongly lensed LBGs brighter than a theoretical survey limit, m_{lim} , is assessed for each of the samples. For the i_{775} , and z_{850} & Y_{105} samples, we assess the lensed fraction brighter than $m_{\text{lim}} = 26, 27, 28, 29$ and 30 mag in H_{160} . We include $m_{\text{lim}} = 25$ mag for the V_{606} sample and $m_{\text{lim}} = 24$ and 25 for the B_{435} sample, as M_* appears brighter for these samples. The strongly lensed fraction is not affected by the differing depth of the CANDELS fields and the XDF.

The cumulative lensed fraction at each of these flux limits is the ratio of the expected number of strongly lensed LBGs (the sum of all lens likelihoods) brighter than the flux limit and the total number of LBGs appearing brighter than the flux limit. However, the cumulative lensed fraction depends on the total completeness of the combined sample. To account for incompleteness in number counts, we use the LF of Bouwens et al. (2014). The cumulative lensed fraction at $z \sim 4, z \sim 5, z \sim 6$ and $z \sim 7$ is shown in the left-hand panel of Fig. 3. The right-hand panel of Fig. 3 shows the observed magnification bias (see Section 6). When inferring properties of the LF (Sections 6.1 and 6.2) we use the observed lensed fraction in each bin without LF-correction so as to not presuppose the nature of the LF.

The trend to a larger fraction of strongly lensed galaxies for brighter flux limits is reasonably smooth, monotonic and observed in each of the four independent samples. The amplitude at all flux limits steadily increases from $z \sim 4$ to $z \sim 7$ (although the error bars are large), which is expected as the faint-end slope steepens and the strong lensing optical depth increases at higher redshift. The excess probability of gravitational lensing of bright galaxies is detected at high significance in each of the samples. The lensed fraction of LBGs brighter than $m_{H_{160}} = 26$ is ~ 6 per cent at $z \sim 7$ and ~ 3.5 per cent at $z \sim 6$, although the uncertainty is large due to the rarity of bright objects at high redshift. At $z \sim 5$, the lensed fraction at the same flux limit is ~ 3.5 per cent and at $z \sim 4$ the lensed fraction is ~ 1.5 per cent.

We also assess the lensed fraction at brighter flux limits for the $z \sim 4$ and $z \sim 5$ samples. We find that the lensed fraction continues to rise, as expected. At $z \sim 5$, ~ 5 per cent of LBGs brighter than $m = 25$ are strongly lensed, and at $z \sim 4$, ~ 4.5 per cent of LBGs brighter than $m = 24$ are lensed.

The errors are calculated using bootstrap resampling. The bootstrap sample is drawn from the entire sample with replacement $N = 10^4$ times. Each time, each LBG is considered either ‘lensed’ or ‘not lensed’ randomly according to its likelihood of having been lensed. The lens fraction is recalculated for all limiting fluxes. The error bars represent the 1σ limits of the resultant distributions.

5.1 Examples of likely lensed systems

We present an illustrative sample of some likely lensed candidates in the surveys in Fig. 2. Cases from our highest- z sample are emphasized because they are of the most interest, and have the most

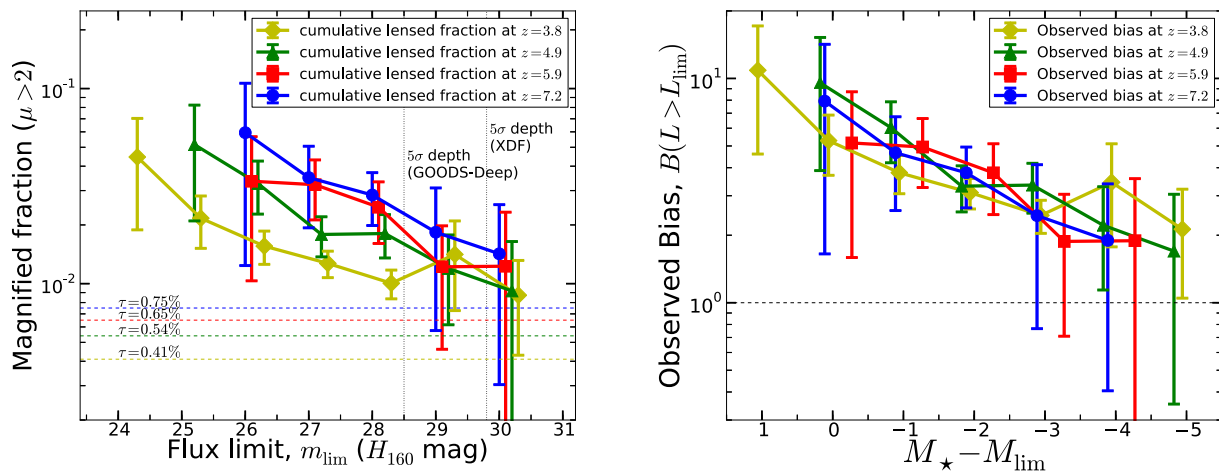


Figure 3. Left: the lensed fraction of background LBGs as a function of flux limit for the z_{850} and Y_{105} -dropout samples (blue), i_{775} -dropouts (red, offset by $m + 0.1$), V_{606} -dropouts (green, offset by $m + 0.2$) and B_{435} -dropouts (yellow, offset by $m + 0.3$). The observed lensed fraction decreases monotonically with decreasing redshift for flux limits of $m_{\text{lim}} = 26, 27, 28$ and 30 . The analytic strong lensing optical depths, τ , (strongly lensed fraction of random lines of sight) for each source redshift are plotted as dashed lines in the same colours as the observed lensed fractions (see Section 6). Right: the observed magnification bias at each redshift overlaid as a function of $M_* - M_{\text{lim}}$ (see Section 6). The B_{435} sample contains the brightest measurements with respect to M_* (1 mag brighter), followed by the V_{606} sample, the z_{850} & Y_{105} sample and the i_{775} sample. The bias is defined as the ratio of the solid and dashed lines in the left-hand panel. We show the bias at each redshift individually in Fig. 5. For an LF without strong evolution in α , which is approximately observed from $4 < z < 7$, the bias is not expected to evolve. A roughly constant bias is observed at all values of $M_* - M_{\text{lim}}$ for the four independent LBG samples from $4 < z < 7$.

importance to future surveys. We note that the three brightest z and Y -dropouts in the entire sample are each deemed to have a likelihood of lensing of >10 per cent. The brightest LBG in the $z \sim 7$ sample is shown in the bottom-left panel of Fig. 2. All cutouts are shown at the same contrast scale, except for the $z \sim 4$ lens candidate (top left), which is in proximity to two very bright foreground galaxies, both with $M_B \sim -23.5$, one of which is spectroscopically confirmed at $z = 0.8$. All cutouts are 10.0 arcsec on each side. In each case, the deflector candidate is labelled with its spectroscopic or photometric redshift and the LBG is labelled with its H_{160} magnitude.

The cutouts highlight the difficulty in locating secondary images in the event the LBG has been strongly lensed. A secondary image will appear closer to the foreground galaxy than the primary (circled) image, and is likely to also appear much fainter than the primary image.

5.2 Deflector properties

We present the distribution of the image–deflector separations, deflector redshifts and deflector B -band absolute magnitudes in this section. The number of lensed sources is weighted by the likelihood of lensing for each image–deflector configuration.

The top row of Fig. 4 shows the distribution of lens rest-frame B -band magnitudes for each of the four independent LBG samples. The peak of the distribution occurs around $M_B \sim -22$ for each of the samples.

The middle row of Fig. 4 shows the distribution of image–deflector separations for each of the LBG samples. The normalized cumulative fractions are shown as dashed lines. We observe an approximate increase in the peak of the separation distribution as redshift increases (from ~ 1.0 arcsec at $z \sim 4$ to ~ 2.0 arcsec at $z \sim 7$), consistent with the expectation that higher redshift sources have larger deflection angles.

The bottom row of Fig. 4 shows the distribution of deflector redshifts. The normalized cumulative fractions are shown as dashed lines. We observe an increase in the peak of the deflector redshift

distribution from $z \sim 4$ sources, where the deflector distribution peaks around $z \sim 1$, to the $z \sim 7$ sources, where the peak occurs around $z \sim 2$. This evolution is consistent with the expectation that lenses are most likely to be found at around half of the angular diameter distance to the source.

6 MAGNIFICATION BIAS

The total magnification bias of a flux-limited sample, $B(L > L_{\text{lim}})$, is the ratio of the fraction of strongly lensed galaxies and the fraction of strongly lensed random lines of sight, defined as the *strong lensing optical depth*, τ (e.g. Wyithe et al. 2011). We generate a catalogue of 50 000 random source positions in the GOODS fields and use the method of assessing the lensed fraction presented above in Section 4 to determine the fraction of the source plane that will be strongly lensed. Based on our FJR, we assess the strong lensing optical depth for sources at $z \sim 4, z \sim 5, z \sim 6$ and $z \sim 7.2$ to be $\tau = 0.41, 0.54, 0.65$ and 0.75 per cent. The values found are broadly consistent with theoretical predictions of the strong lensing optical depths at these redshifts (Barkana & Loeb 2000; Wyithe et al. 2011; Mason et al. 2015). Due to the large number of foregrounds in the CANDELS fields, the relative statistical uncertainty on τ is only ~ 4 per cent in all samples, and hence negligible in our bias calculations. We find consistent values for the optical depth if we apply a reasonable upper limit of $\sim 350 \text{ km s}^{-1}$ on the inferred velocity dispersion of foreground galaxies. We find that our method of determining the optical depth returns values in close agreement with those in Mason et al. (2015) when we adopt their method of inferring velocity dispersions using stellar mass estimates.² The optical depths are plotted as dashed lines in Fig. 3.

The bias is therefore the observed magnified fraction divided by the optical depth (the solid lines divided by the dashed lines in

²We use stellar mass estimates of foreground galaxies in the GOODS/CANDELS fields from the 3D-HST catalogue.

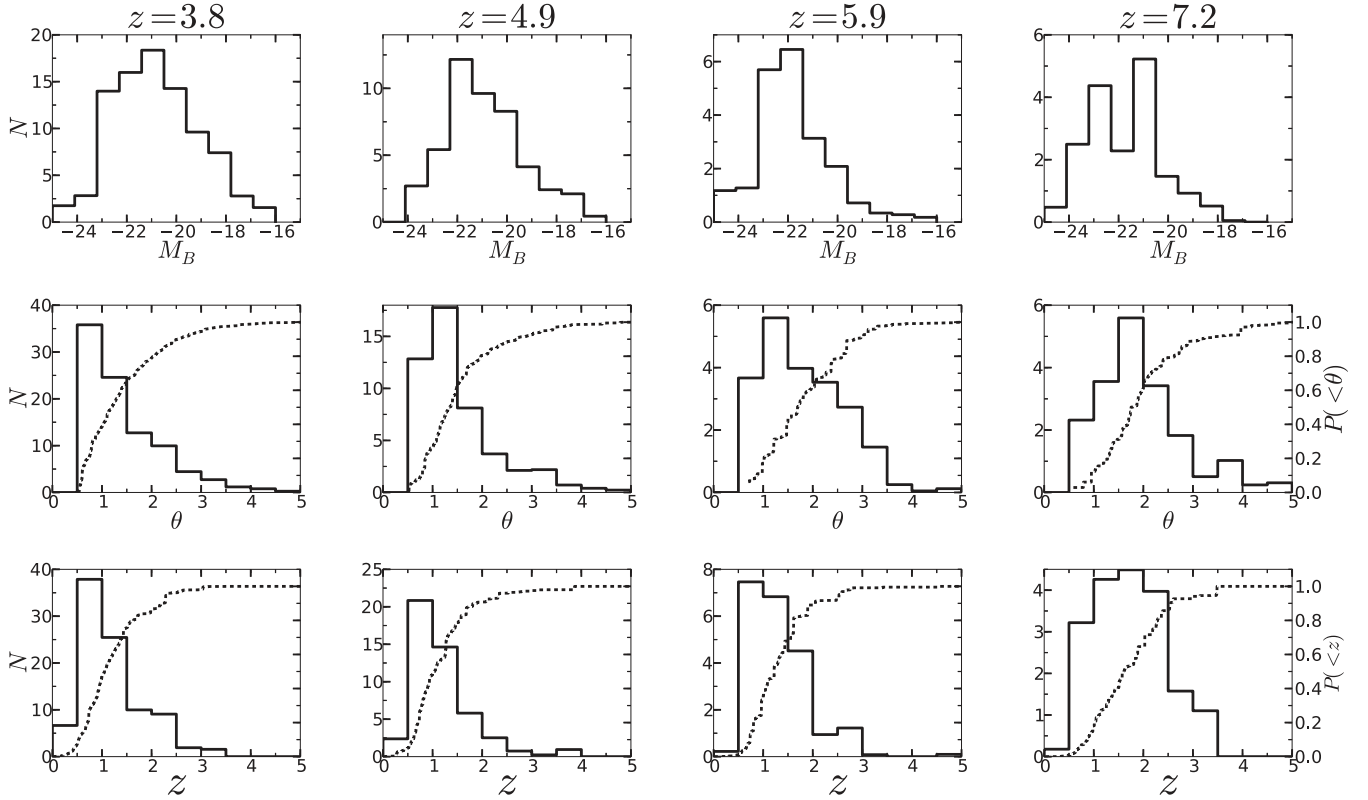


Figure 4. The lensing-likelihood-weighted distributions (solid) and cumulative distributions (dashed) of deflector properties. These distributions illustrate the diversity and evolution of the deflector population in the four samples analysed. Top row: the distribution of B -band absolute magnitudes of the deflectors for the four LBG samples. Middle row: the distribution of image–deflector separations for the four LBG samples. Bottom row: the distribution of redshifts of the deflectors for the four LBG samples.

Fig. 3). The observed total bias for each of the samples at a range of flux limits is plotted in the right-hand panel of Fig. 3 and the top row of Fig. 5. The bias reaches values of ~ 10 at bright magnitudes and high redshifts, but near the survey flux limit has values lower than expected for a LF that remains steep well beyond survey limits.

We calculate the observed magnification bias in each bin (as opposed to the total magnification bias for all galaxies brighter than a flux limit). The results are plotted in the bottom row of Fig. 5.

For an LF with weak (or no) redshift evolution of the α parameter, the magnification bias as a function of $M_* - M_{\text{lim}}$ is expected to remain approximately constant with redshift. To highlight that this trend exists in the data, we plot the observed magnification bias at each redshift on the same axes in the right-hand panel of Fig. 3. While α evolves from ~ -1.6 to ~ -2.0 from $z \sim 4$ to $z \sim 8$, the statistical uncertainties in our measurements are larger than the change in bias from this evolution.

For a given LF, $\Psi(L)$, the magnification bias can be predicted analytically (Turner et al. 1984) at luminosity L , by

$$B(L) = \frac{\int_{\mu_{\text{min}}}^{\mu_{\text{max}}} \frac{d\mu}{\mu} \frac{dP}{d\mu} \Psi(L/\mu)}{\Psi(L)}, \quad (8)$$

where the $1/\mu$ factor accounts for the stretching of $\Psi(L/\mu)d\mu$ with magnification, and $\frac{dP}{d\mu}$ is the magnification distribution for the brighter image in a strongly lensed system, given for an SIS by

$$\frac{dP}{d\mu} = \begin{cases} \frac{2}{(\mu-1)^3} & \text{for } 2 < \mu < \infty \\ 0 & \text{for } \mu < 2 \end{cases}. \quad (9)$$

We assume $\Psi(L)$ to be the Schechter LF. The analytic magnification bias for all galaxies in a flux-limited sample is

$$B(L > L_{\text{lim}}) = \frac{\int_{\mu_{\text{min}}}^{\mu_{\text{max}}} d\mu \int_{L_{\text{lim}}}^{\infty} dL \frac{dP}{d\mu} \Psi(L/\mu)}{\int_{L_{\text{lim}}}^{\infty} dL \Psi(L)}, \quad (10)$$

where the factor of $1/\mu$ is no longer included because we are now integrating over luminosity, and hence the luminosity limits are also stretched by μ in the numerator.

Results for our bias estimates given the Schechter LF parameters in Bouwens et al. (2014) and theoretical curves are plotted in Fig. 5. The top row compares the theoretical bias of all galaxies in a flux-limited sample with our measurements of the observed bias for all galaxies in a flux-limited sample. The bottom row shows the theoretical bias of galaxies at a fixed luminosity with our measurements of the observed bias in each magnitude bin. Theoretical values for bias are calculated using previously derived LF parameters α and M_* (Bouwens et al. 2014) and a range of values at which the LF deviates from a steep faint-end slope. We find close agreement between the observed shape and amplitude of the magnification bias and the theoretical function in each of the independent samples.

It is worth noting that the inferred magnification bias is not sensitive to the parameters of the FJR (Section 3), because the use of the FJR to determine the efficiency of observed galaxies affects both the numerator (fraction of strongly lensed LBGs) and the denominator (the strong lensing optical depth) similarly.

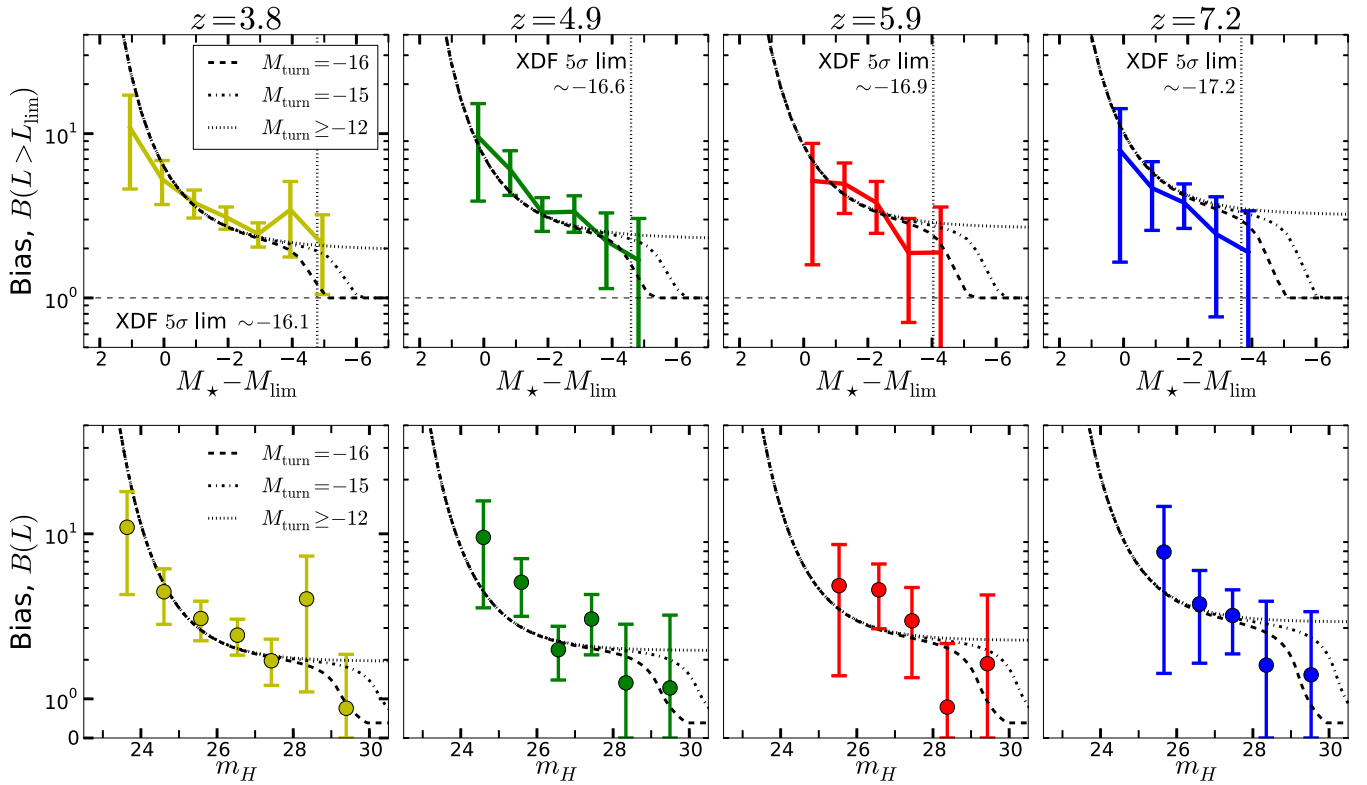


Figure 5. Top row: the observed total magnification bias of all galaxies brighter than a flux limit $M_* - M_{\text{lim}}$ (solid) compared with the theoretical magnification bias for the LFs (described by equation 10) from Bouwens et al. (2014) with a range of magnitudes at which the LF flattens ($\alpha \sim -1$), denoted by M_{turn} . The cumulative lensed fraction is corrected for incompleteness according to the LF of Bouwens et al. (2014). Bottom row: the observed magnification bias in each bin plotted at the mean luminosity of the bin. At faint magnitudes in each sample of LBGs, the bias falls below the value expected from a faint-end slope continuing well beyond the survey limit, indicating a possible deviation from a steep faint-end slope of the LF, although they agree with theory within their error bars. For an LF with a steep faint-end slope continuing well beyond the flux limit, the bias flattens to a value of $B \sim 2\text{--}3$ (depending on α). The measurements of bias at a fixed luminosity do not need to be corrected for incompleteness.

6.1 The faint-end slope beyond current flux limits

Magnification bias results from magnification of intrinsically faint sources below an observed flux limit into an observed sample, hence quantifying the degree of magnification bias offers an opportunity to investigate the behaviour of the LF beyond current survey limits.

To illustrate, we begin with a toy model in which there is a minimum luminosity for galaxies of L_{min} , below which there are no galaxies, and a power-law slope of $\alpha = -2.0$ for $L > L_{\text{min}}$. In this toy model, a sharp cutoff in the LF at a value of L_{min} yields a bias

$$B(L > L_{\text{lim}}) = \begin{cases} 3 - \frac{2}{L_{\text{lim}}/L_{\text{min}} - 1} & \text{for } L_{\text{lim}} > 2L_{\text{min}} \\ 1 & \text{for } L_{\text{min}} < L_{\text{lim}} < 2L_{\text{min}} \end{cases} \quad (11)$$

This implies the total bias of a flux-limited sample reaches unity approximately 1 mag brighter than L_{min} . We observe a hint of the possibility of this occurring in the four samples presented in this paper, as seen in the top row of Fig. 5. The bottom row of Fig. 5 also highlights this behaviour in our samples.

Rather than a sharp cutoff in the LF, we consider a more realistic model with an LF that flattens ($\alpha_2 = -1$) after some luminosity, L_{turn} . We attempt to constrain L_{turn} by finding an LF that will reproduce the observed magnification bias in the bot-

tom row of Fig. 5. Using a broken Schechter function of the form

$$\Psi(L)dL = \begin{cases} \Psi_{*,1} \left(\frac{L}{L_*}\right)^{\alpha_1} \exp\left(-\frac{L}{L_*}\right) \frac{dL}{L_*} & \text{for } L \geq L_{\text{turn}} \\ \Psi_{*,2} \left(\frac{L}{L_*}\right)^{\alpha_2} \exp\left(-\frac{L}{L_*}\right) \frac{dL}{L_*} & \text{for } L < L_{\text{turn}}, \end{cases} \quad (12)$$

with $\alpha_2 = -1$ (i.e. a flat LF beyond L_{turn}), we fit the bias calculated from equation (8) to the data with L_{turn} , α_1 and M_* as free parameters. We include priors on the values of α_1 and M_* , from the LFs of Bouwens et al. (2014). Fig. 6 shows the constraints found for the minimum luminosity from our analysis fitting to two subsets of our measurements. The dashed black line in Fig. 6 shows the probability distribution function (PDF) when fitting M_{turn} to the observed bias of only LBGs brighter than $m = 29$, and the solid line shows the PDF when fitting to LBGs brighter than $m = 30$ (approximately the 5 σ limit in the XDF). The PDFs are normalized such that the probability of $M_{\text{turn}} < -12$ is unity. We find preferred values of M_{turn} to peak around the current observational limits in each of the independent samples from $4 < z < 7$. The sample at $z \sim 6$ peaks at a magnitude brighter than flux limits, which can be ruled out observationally. We also calculate the likelihoods with an additional prior enforcing M_{turn} to occur below the magnitude that the steep faint-end slope has been observed to extend to. These are plotted in red in Fig. 6 for the same flux limits as above. It is important to note that the

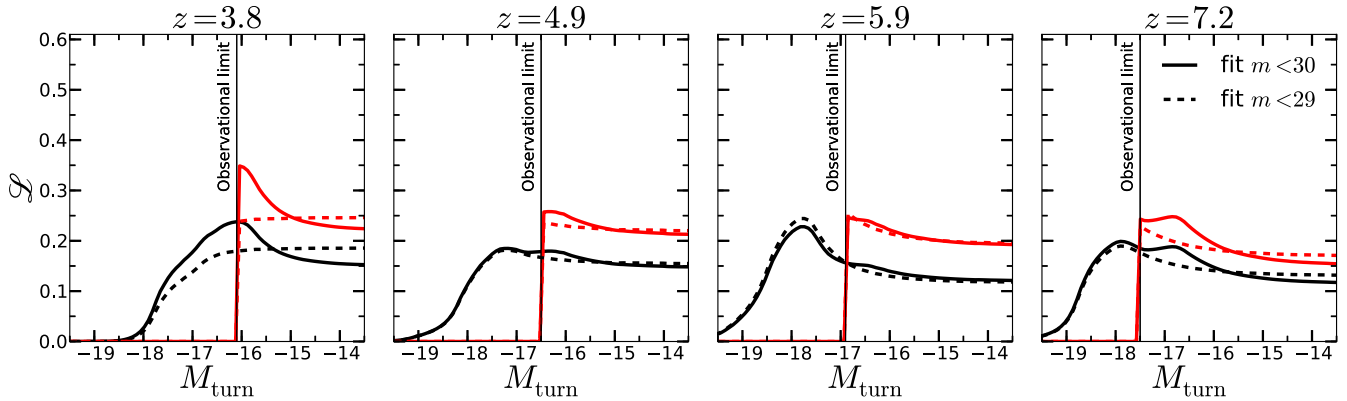


Figure 6. The inferred value of M_{turn} using the magnification bias measurements of all galaxies brighter than $m < 30$ (solid) and all galaxies brighter than $m < 29$ (dashed). The bias measurements which we fit to are shown in the bottom row of Fig. 5. In black we plot the likelihoods with a prior on α and M_* from Bouwens et al. (2014, see table 4 therein for values). The red curves show the estimated likelihoods including an additional requirement that the minimum magnitude is fainter than the magnitude to which current observations confirm a steep faint-end slope. We find approximately consistent preferred values of M_{turn} in each of the four samples, but with varying amplitudes. For LBGs brighter than $m = 30$ (approximately the 5σ XDF limit, solid line), we find a preferred value of M_{turn} around the observational limits in each sample. However, a value of $M_{\text{turn}} > -16$ is not excluded. For only LBGs brighter than $m = 29$ (dashed line), we find no constraint on M_{turn} in any of the samples. This is expected, because to constrain M_{turn} we need to consider galaxies within ~ 1 – 2 mag of M_{turn} . The curves are normalized such that the probability of $M_{\text{turn}} < -12$ is unity.

inference of M_{turn} occurring close to current flux limits is marginal and does not rule out a faint-end slope extending well beyond current flux limits, or a flattening for a few magnitudes followed by an upturn.

We find that the constraint disappears when M_{turn} is fitted to only brighter ($m < 29$) galaxies. We extend this test by recalculating our results by omitting XDF LBGs entirely from the analysis to investigate whether the observed magnification bias will always approach unity near the flux limit due to selection effects. When we perform this test, we find the magnification bias of galaxies in the GOODS-North and GOODS-South is completely consistent with that of the full sample, rather than approaching unity near the flux limit.

It is important to note that the magnification bias is only observed to drop below its expected value close to the current flux limits where selection effects become significant. While we have taken care to account for the decreased sensitivity to very faint sources, there still exists the possibility that we have missed a significant fraction of gravitationally lensed LBGs at very faint magnitudes. Furthermore, if the interloper fraction at very faint fluxes is high, the lensed fraction will be underestimated, causing a spurious inference of M_{turn} .

The possibility of a flattening of the LF at $M_{\text{turn}} \sim -16.5$ at $z \sim 7$ is consistent with observations of LBGs down to $M_{\text{UV}} \sim -15.5$ of magnified $z \sim 7$ LBGs using Frontier Fields cluster Abell 2744 (Atek et al. 2015; Ishigaki et al. 2015). Fig. 7 shows the Bouwens et al. (2014) and Atek et al. (2015) data with the best-fitting broken Schechter function ($\alpha_2 = -1$). We find that a broken Schechter function represents the data very well, and offers an independent constraint on M_{turn} . The data favour a value of $M_{\text{turn}} \sim -16.5$, consistent with M_{turn} inferred from our magnification bias results. However, as is the case with our magnification bias analysis, this inference is based on a single data point.

Further to this study at $z \sim 7$, there exist measurements of the UV LF of $z \sim 2$ LBGs down to $M_{\text{UV}} \sim -13$ (Alavi et al. 2014). While a single Schechter function favours a steep slope extending to $M_{\text{UV}} \sim -13$ at $z \sim 2$, the shape of the LF at the faint end may be more complicated than this simple parametrization. In fact, the data also seem to suggest a flattening of the population density between

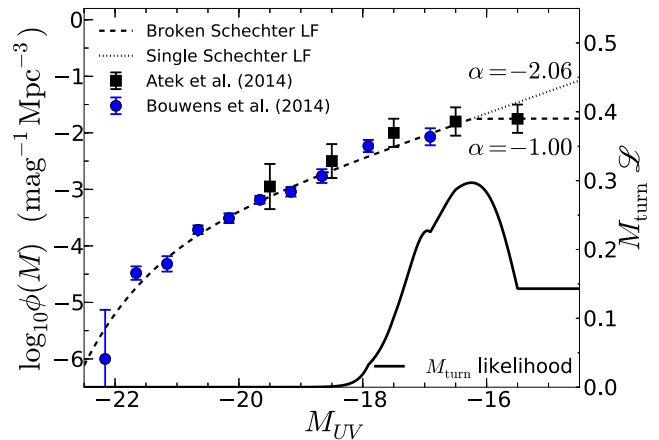


Figure 7. The $z \sim 7$ LF data from Bouwens et al. (2014, blue circles) and Atek et al. (2015, black squares) with the best-fitting broken Schechter LF (dashed) and single Schechter LF (dotted). The solid line shows the likelihood of M_{turn} given the two data sets. We find a favoured flattening magnitude at $M_{\text{UV}} \sim -16.5$, consistent with our magnification bias measurements.

$-17 \lesssim M_{\text{UV}} \lesssim -15$, before a steeper upturn from $-15 \lesssim M_{\text{UV}} \lesssim -13$ (see Alavi et al. 2014, fig. 7). This more complicated LF would produce a reduced magnification bias ($B(L > L_{\text{lim}}) \sim 1$) of $z \sim 2$ LBGs near a flux limit of $M_{\text{UV}} \sim -17.5$, which is on the edge of current survey limits in blank fields (Reddy & Steidel 2009; Hathi et al. 2010; Oesch et al. 2010; Sawicki 2012). Additionally, a flattening, and potentially a rise in the LF at $M_{\text{UV}} \gtrsim -15$ would not be inconsistent with the inference from GRB host galaxies studies (Tanvir et al. 2012; Trenti et al. 2012; Trenti, Perna & Tacchella 2013). In fact, these studies only constrain the presence of an abundant population of galaxies below the XDF detection limit, but not the shape of the galaxy LF, which they assume to be Schechter-like. Interestingly, theoretical models that are based on a double population of faint galaxies have been proposed in the context of hydrogen reionization (e.g. see Alvarez, Finlator & Trenti 2012).

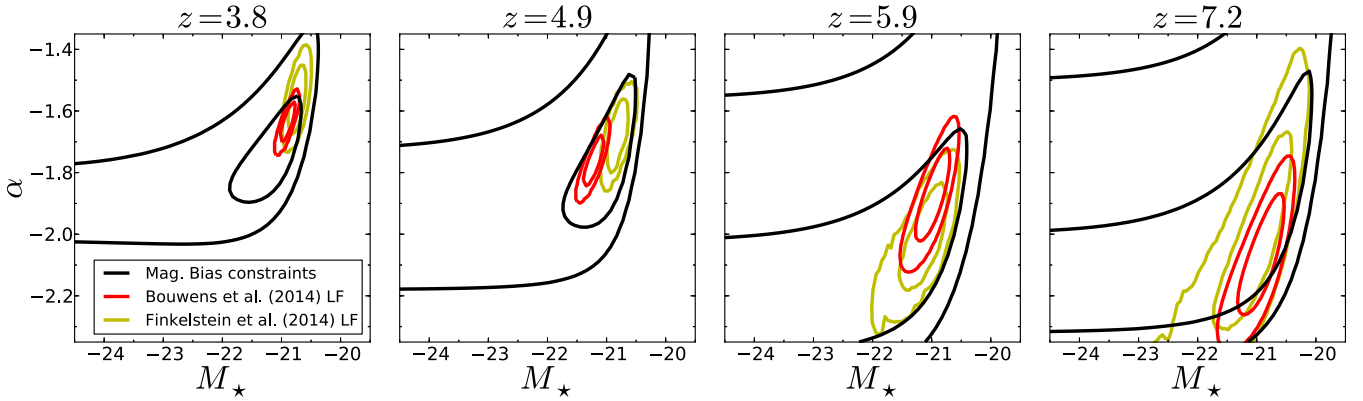


Figure 8. Measurement of the Schechter parameters, α and M_* , using only the observed magnification bias as a function of $M_* - M_{\text{lim}}$ (black). The contours from Bouwens et al. (2014, red) and Finkelstein et al. (2014, yellow) LF are shown for comparison. We find close agreement between the two methods at $z \sim 4$ and $z \sim 5$, while the constraints at $z \sim 6$ and $z \sim 7$ from lensing are weaker due to the larger error bars on the magnification bias measurements.

6.2 Deriving Schechter parameters from lensing

A very interesting application of this analysis is that Schechter function parameters α and M_* can be derived directly from the magnification bias. This method is completely independent of the standard procedure using number counts of galaxies, and therefore could be combined to produce improved constraints.

The magnification bias at a fixed luminosity can be predicted using equation (8), and is a function of α and M_* . By fitting the predicted bias of LBGs at a fixed flux to our measured bias in each flux bin (which is shown in the bottom row of Fig. 5, and is not the LF-corrected cumulative fraction), we can constrain α and M_* .³ This does not rely on any prior knowledge of the LF. Because α and M_* are much more sensitive to the bias of bright galaxies than that of faint galaxies, and we see a possible deviation from a single Schechter function at faint magnitudes, we exclude the two faintest bins ($29 < m < 30$, and $28 < m < 29$) from the fit.⁴ Fig. 8 shows the constraints on the LF from the observed magnification bias alone along with the constraints from number counts of the same samples.

The measurements of the bias at $z \sim 4$ and $z \sim 5$ do an excellent job of constraining the LF. At higher redshift, as the samples become smaller and the random errors grow, we cannot constrain the LF as effectively. However, we find that our observations are consistent with the UV LFs presented by Bouwens et al. (2014). This also provides an internal consistency check of our analysis.

6.3 Contaminant discussion

We check for bias arising from the selection of LBGs. There may be an enhancement and reddening of LBG candidates observed around bright, red foreground galaxies due to photometric scatter, causing an increased fraction of interlopers around such foreground objects and providing a false lensing signal among bright candidates. To determine if this may affect our results, we check if an enhanced interloper fraction around bright foregrounds is found in lower redshift LBG samples for which there exists spectroscopic follow-up.

³ We fit the theoretical bias at the mean magnitude of the LBGs in each magnitude bin to the observed bias in that bin with α and M_* as free parameters.

⁴ In fact, fitting the data including the two faintest bins with an extra free parameter, M_{turn} , and marginalizing over this parameter gives the same result.

We combine catalogues with spectroscopically confirmed LBGs and photometrically selected LBGs which were identified as interlopers from $3 < z < 6$ using observations reported by Vanzella et al. (2009), Reddy et al. (2006), Malhotra et al. (2005) and Steidel et al. (2003). We compare the fraction of interlopers for LBGs within 5.0 arcsec of bright, red foreground galaxies ($m_r < -22$ mag) with the fraction of interlopers in the total sample. In both cases, we find the interloper fraction to be ~ 8 per cent, with 2 of 25 LBGs around bright foreground galaxies identified as interlopers, and 21 of 252 of the entire sample. This indicates that the alignment between bright LBGs and massive foreground galaxies is not likely due to selection bias. The large enhancement in false identifications required to mimic the observed magnification bias of ~ 10 for bright galaxies is clearly inconsistent with the spectroscopic data.

7 MAGNIFICATION BIAS AND THE LF

The effect of magnification bias on determining the LF is an important consideration when making a census of galaxies in the epoch of reionization (Wyithe et al. 2011; Mason et al. 2015). In this section, we show the effect that the lensed fraction reported in this paper has on the observed LF.

The observed LF of LBGs is the convolution between the intrinsic LF, $\Psi(L)$, and the magnification distribution of an SIS, $\frac{dP}{d\mu}$, weighted by the strong lensing optical depth, τ . This results in an observed LF, $\Psi_{\text{obs}}(L)$, with a power-law tail at the bright end with a slope of -3 (the slope of the magnification distribution of an SIS). We assess the effect of gravitational lensing on the LF by following the method presented by Wyithe et al. (2011), where it is modelled by considering the optical depth, τ , the mean magnification of multiply imaged sources for an SIS, $\langle \mu_{\text{mult}} \rangle = 4$, and the demagnification of unlensed sources (to conserve total flux on the cosmic sphere), $\mu_{\text{demag}} = (1 - \langle \mu_{\text{mult}} \rangle \tau) / (1 - \tau)$. The observed LF is then given by

$$\Psi_{\text{obs}}(L) = (1 - \tau) \frac{1}{\mu_{\text{demag}}} \Psi(L/\mu_{\text{demag}}) + \tau \int_0^\infty d\mu \frac{1}{\mu} \left(\frac{dP_{m,1}}{d\mu} + \frac{dP_{m,2}}{d\mu} \right) \Psi(L/\mu), \quad (13)$$

where $\frac{dP_{m,2}}{d\mu} = 2/(\mu + 1)^3$ for $0 < \mu < \infty$ is the second image's magnification probability distribution, and $\frac{dP_{m,1}}{d\mu}$ is given by equation (9). We use the values of the optical depth from our analysis

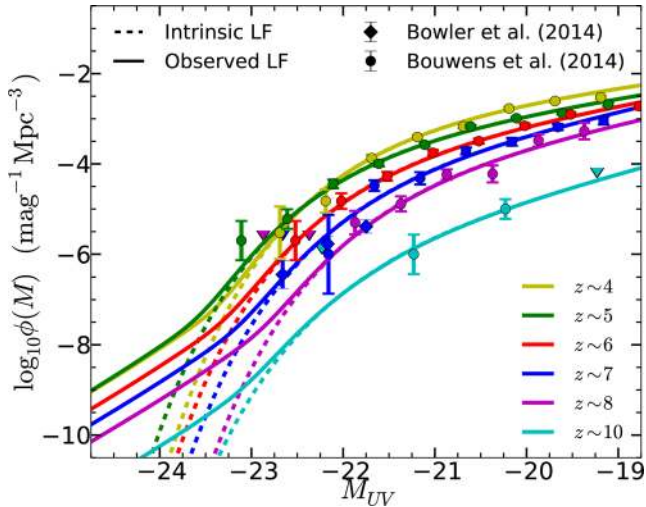


Figure 9. The effect of magnification bias on the bright end of the LFs $z \sim 4$, $z \sim 5$, $z \sim 6$, $z \sim 7$, $z \sim 8$ and $z \sim 10$ (LBGs become monotonically more abundant with decreasing redshift at $M_{UV} \leq -22$). The observed LFs are shown as solid lines, and the intrinsic LFs as dashed lines. The LF measurements from Bouwens et al. (2014) and Bowler et al. (2014) are plotted as circles and diamonds, respectively. At $z \sim 7$, $z \sim 8$ and $z \sim 10$, observations are close to probing the bright end where gravitational lensing becomes a significant effect, but not bright enough for it to be manifested in the observed LF.

presented in Section 6, and calculate the optical depth at $z = 6.8$, $z = 7.9$ and $z = 10.4$ to be $\tau = 0.72$, 0.80 and 0.94 per cent, respectively.

We begin by assuming that the observed LF is not affected by gravitational lensing and hence represent the intrinsic LFs. We plot these intrinsic LFs (Bouwens et al. 2014), the inferred observed LF and observations (Bouwens et al. 2014; Bowler et al. 2014) at $z \sim 4$, $z \sim 5$, $z \sim 6$, $z \sim 7$, $z \sim 8$ and $z \sim 10$ in Fig. 9 (dashed lines). Fig. 9 also shows the biased LFs, illustrating the luminosity at which gravitational lensing becomes important. This also illustrates the assumption that current LF measurements are not significantly affected by magnification bias is sound.

The effect of magnification bias is not significant at the faint end of the LF. At around 2 mag fainter than M_* , the excess observed abundance of LBGs is of the order of 0.5 per cent for all of the samples, which is significantly smaller than the observational errors in the abundances at these magnitudes.

We note that even the brightest Bowler et al. (2014) and Bouwens et al. (2014) measurements are not bright enough to probe the affected region of the LF. However, the effect magnification bias will have on surveys at $z \gtrsim 8$ is obvious from the solid lines for $z \sim 8$ and $z \sim 10$ where the observed LF will display a break from the intrinsic LF around $M_{UV} \lesssim -22.5$.

Not plotted in Fig. 9 are extrapolated LFs at $z > 10$. Wytke et al. (2011) showed that if M_* drops sharply at high redshifts, surveys of the depth of the XDF with *JWST* will observe galaxies at $z > 10$ in the affected region of the LF.

8 ANALYSIS OF CURRENT J_{125} -DROPOUTS

In Section 7, we presented the effect that magnification bias has on the observed LF. Fig. 9 highlights that while magnification bias is not a significant effect in current surveys out to $z \sim 8$, the affected region of the $z \sim 10$ LF begins at around $M_{UV} \sim -22.5$. We investigated the four unusually bright $z \sim 10$ J_{125} -dropouts pre-

sented by Oesch et al. (2014) to search for evidence of lensing. This point is discussed in Oesch et al. (2014), where they find there is the possibility of a modest amount of lensing in two of the four dropouts. By applying the technique employed in this paper, we assign likelihoods of lensing to the four $z \sim 9$ – 10 LBGs.

As noted by Oesch et al. (2014), two of the LBGs are not close in projection to any foreground objects (GN-z10-3 and GN-z9-1 in the notation of Oesch et al. 2014), while the other two do have projected neighbours (GN-z10-1 and GN-z10-2). GN-z10-1 is 1.2 arcsec from a foreground galaxy at $z_{\text{phot}} = 1.6$ with $M_B = -20.1$ (using photometry from the 3D-HST catalogue). Oesch et al. (2014) infer a photometric redshift of $z = 1.8$). Using our redshift-evolving FJR, this corresponds to a stellar velocity dispersion of 140 km s^{-1} . The required stellar velocity dispersion for strong-lensing in this case is 198 km s^{-1} , giving this LBG a likelihood of lensing of $\mathcal{L} = 0.12$. GN-z10-2 is 2.9 arcsec from a bright galaxy at $z_{\text{spec}} = 1.02$ with $M_B = -20.7$. This corresponds to an inferred stellar velocity dispersion of 214 km s^{-1} . The required stellar velocity dispersion for strong lensing is 279 km s^{-1} , giving a likelihood of lensing of $\mathcal{L} = 0.1$. While the statistics are too small to draw any firm conclusions, this average observed lensed fraction of ~ 6 per cent for the four galaxies is consistent with a lensed fraction of LBGs brighter than M_* of ~ 10 per cent.

9 SUMMARY

We have estimated the likelihood of strong gravitational lensing of LBGs in the XDF and GOODS at $z \sim 4$, $z \sim 5$, $z \sim 6$ and $z \sim 7$. We used a calibrated FJR to estimate the lensing potential of all foreground objects in the fields. The result is a measurement of significant magnification bias in current high-redshift samples of LBGs. Our analysis allows us to draw the following conclusions.

- (i) Approximately 6 per cent of LBGs at $z \sim 7$ brighter than M_* ($m_{H160} \sim 26$ mag) are expected to have been strongly gravitationally lensed with $\mu > 2$.
- (ii) The observed strongly lensed fraction of LBGs at all values of m_{H160} falls monotonically from $z \sim 7$ to $z \sim 4$, which can be explained by the expected evolution in the optical depth with redshift, and also M_* appearing brighter at lower redshift.
- (iii) By evaluating the optical depth in our lensing framework, we calculate the magnification bias in each sample as a function of $M_* - M_{\text{lim}}$, and find that the results agree at each redshift and are well described by theoretical predictions.
- (iv) Extrapolation of our analysis leads to expectations for an increased fraction of strongly lensed galaxies at $z \gtrsim 8$, consistent with Wytke et al. (2011).
- (v) The magnification bias of the faintest LBGs in the sample suggests there may be a flattening of the faint-end slope below current detection limits ($M_{UV} \gtrsim -16.5$). However, this result relies on LBG detections at low S/N in the XDF, and the constraints are weak. We present this result tentatively, with deeper data needed to better understand the population of faint high- z galaxies.
- (vi) Assessing the magnification bias as a function of luminosity offers an independent method of determining Schechter parameters α and M_* . The results from this method are consistent with those found by fitting the LF based on number counts.

With the confirmation of the role of magnification bias come important consequences for future surveys of galaxies at $10 < z < 20$. Currently, the LFs at $z \sim 8$ need not be corrected for magnification bias. However, magnification bias will be significant for LFs at $z \gtrsim 10$, notably in the *JWST* era (Wytke et al. 2011). In particular,

with M_* possibly dropping rapidly beyond $z \sim 8$ (Oesch et al. 2014), *JWST* will identify predominantly gravitationally lensed galaxies at $z \gtrsim 10$.

ACKNOWLEDGEMENTS

JSBW is supported by an Australian Research Council Australian Laureate Fellowship. MT acknowledges support from the Australian Research Council through the award of a Future Fellowship. TT acknowledges support from the Packard Foundation via a Packard Fellowship. We thank Charlotte Mason for her useful comments and conversations. We also thank Adriano Fontana for his useful comments and suggestions.

REFERENCES

- Alavi A. et al., 2014, *ApJ*, 780, 143
 Alvarez M. A., Finlator K., Trenti M., 2012, *ApJ*, 759, L38
 Ashby M. et al., 2013, *ApJ*, 769, 80
 Atek H. et al., 2015, *ApJ*, 800, 18
 Auger M., Treu T., Bolton A., Gavazzi R., Koopmans L., Marshall P., Bundy K., Moustakas L., 2009, *ApJ*, 705, 1099
 Barkana R., Loeb A., 2000, *ApJ*, 531, 613
 Barmby P., Huang J.-S., Ashby M., Eisenhardt P., Fazio G., Willner S., Wright E., 2008, *ApJS*, 177, 431
 Barone-Nugent R., Wyithe J., Trenti M., Treu T., Oesch P., Bradley L., Schmidt K., 2013, preprint (arXiv:1303.6109)
 Bernardi M. et al., 2003, *AJ*, 125, 1849
 Bielby R. et al., 2012, *A&A*, 545, A23
 Bouwens R. J., Illingworth G. D., Franx M., Ford H., 2008, *ApJ*, 686, 230
 Bouwens R. et al., 2011, *ApJ*, 737, 90
 Bouwens R. et al., 2014, preprint (arXiv:1403.4295)
 Bowler R. et al., 2014, *MNRAS*, 440, 2810
 Bradley L. et al., 2012, *ApJ*, 760, 108
 Brammer G. B., van Dokkum P. G., Coppi P., 2008, *ApJ*, 686, 1503
 Brammer G. B. et al., 2012, *ApJS*, 200, 13
 Calvi V., Pizzella A., Stiavelli M., Morelli L., Corsini E., Dalla Bontà E., Bradley L., Koekemoer A., 2013, *MNRAS*, 432, 3474
 Castellano M. et al., 2010, *A&A*, 524, A28
 Comerford J. M., Haiman Z., Schaye J., 2002, *ApJ*, 580, 63
 Erben T. et al., 2009, *A&A*, 493, 1197
 Faber S., Jackson R. E., 1976, *ApJ*, 204, 668
 Finkelstein S. L. et al., 2012, *ApJ*, 758, 93
 Finkelstein S. L. et al., 2014, preprint (arXiv:1410.5439)
 Grogin N. A. et al., 2011, *ApJS*, 197, 35
 Hathi N. et al., 2010, *ApJ*, 720, 1708
 Hoekstra H., Yee H. K., Gladders M. D., 2004, *ApJ*, 606, 67
 Huterer D., Keeton C. R., Ma C.-P., 2005, *ApJ*, 624, 34
 Hyde J. B., Bernardi M., 2009a, *MNRAS*, 394, 1978
 Hyde J. B., Bernardi M., 2009b, *MNRAS*, 396, 1171
 Illingworth G. et al., 2013, *ApJS*, 209, 6
 Ishigaki M., Kawamata R., Ouchi M., Oguri M., Shimasaku K., Ono Y., 2015, *ApJ*, 799, 12
 Jönsson J., Dahlén T., Hook I., Goobar A., Mörtzell E., 2010, *MNRAS*, 402, 526
 Keeton C. R., 2001, preprint (astro-ph/0102341)
 Khochfar S., Silk J., Windhorst R., Ryan R., Jr, 2007, *ApJ*, 668, L115
 Kleinheinrich M. et al., 2006, *A&A*, 455, 441
 Koekemoer A. M. et al., 2011, *ApJS*, 197, 36
 Kormann R., Schneider P., Bartelmann M., 1994, *A&A*, 284, 285
 McCracken H. et al., 2012, *A&A*, 544, A156
 McLure R. et al., 2006, *MNRAS*, 372, 357
 McLure R. et al., 2013, *MNRAS*, stt627
 Malhotra S. et al., 2005, *ApJ*, 626, 666
 Mashian N., Loeb A., 2013, *J. Cosmol. Astropart. Phys.*, 12, 017
 Mason C. et al., 2015, preprint (arXiv:1502.03795)
 Newman A. B., Ellis R. S., Treu T., Bundy K., 2010, *ApJ*, 717, L103
 Oesch P. et al., 2010, *ApJ*, 725, L150
 Oesch P. et al., 2012, *ApJ*, 759, 135
 Oesch P. et al., 2014, *ApJ*, 786, 108
 Oke J., Gunn J., 1983, *ApJ*, 266, 713
 Pei Y. C., 1995, *ApJ*, 440, 485
 Reddy N. A., Steidel C. C., 2009, *ApJ*, 692, 778
 Reddy N. A., Steidel C. C., Erb D. K., Shapley A. E., Pettini M., 2006, *ApJ*, 653, 1004
 Robertson B. E. et al., 2013, *ApJ*, 768, 71
 Sawicki M., 2012, *MNRAS*, 421, 2187
 Schenker M. A. et al., 2013, *ApJ*, 768, 196
 Schmidt K. B. et al., 2014, *ApJ*, 786, 57
 Skelton R. E. et al., 2014, *ApJS*, 214, 24
 Steidel C. C., Adelberger K. L., Shapley A. E., Pettini M., Dickinson M., Giavalisco M., 2003, *ApJ*, 592, 728
 Taniguchi Y. et al., 2007, *ApJS*, 172, 9
 Tanvir N. et al., 2012, *ApJ*, 754, 46
 Trenti M., Perna R., Levesque E. M., Shull J. M., Stocke J. T., 2012, *ApJ*, 749, L38
 Trenti M., Perna R., Tacchella S., 2013, *ApJ*, 773, L22
 Treu T. et al., 2005, *ApJ*, 633, 174
 Turner E. L., Ostriker J. P., Gott J. R., III, 1984, *ApJ*, 284, 1
 Vanzella E. et al., 2009, *ApJ*, 695, 1163
 Whitaker K. E. et al., 2011, *ApJ*, 735, 86
 Windhorst R. A. et al., 2011, *ApJS*, 193, 27
 Wyithe J. S. B., Yan H., Windhorst R. A., Mao S., 2011, *Nature*, 469, 181
 Yue B., Ferrara A., Vanzella E., Salvaterra R., 2014, *MNRAS*, 443, L20

APPENDIX A: SPATIAL CORRELATIONS BETWEEN BRIGHT FOREGROUNDS AND LBGs

In this appendix, we present the manifestation of magnification bias in spatial correlations between bright foreground objects and bright LBGs, which illustrates the effect without relying on the FJR.

Source galaxies that have been magnified through gravitational lensing are necessarily located in close proximity to massive foreground objects. For the lensed fractions presented in Section 5, we expect there to be an excess density of bright LBGs around bright foreground objects over the average field density. As the lensed fraction decreases with decreasing luminosity, the excess probability around bright deflectors should also decrease. Similarly, the clustering around the more massive, brighter deflectors should be stronger than around less massive, fainter deflectors.

We compute the excess probability of finding an LBG brighter than $m = 30, 28.5, 27.5$ and 26.5 at $\bar{z} = 7.2$ within 5.0 arcsec of deflectors brighter than some M_B . We choose 5.0 arcsec as our limit as this is approximately the image–deflector separation beyond which strong lensing is unlikely. This is confirmed by the distribution of separations shown in Fig. 4. We also present the spatial correlations for the lower redshift samples. At $\bar{z} = 5.9$, we examine the same flux limits, at $\bar{z} = 4.9$ we replace $m_{\text{lim}} = 30$ with $m_{\text{lim}} = 25.5$ and at $\bar{z} = 3.8$ we replace $m_{\text{lim}} = 28.5$ with $m_{\text{lim}} = 24.5$. The results are plotted in Fig. A1.

We find a large enhancement in the probability of finding bright LBGs nearby bright deflectors. As we consider fainter LBGs, the excess probability decreases monotonically in all of the samples. There exists a considerable excess of LBGs around foregrounds with $M_B < -23$ at $z \geq 4$, even for flux limits well beyond M_* ; however, this signal is driven mainly by the brightest LBGs. The excess likelihood of locating an LBG around a foreground approaches unity by $M_B \sim -21$ for all flux limits in all samples.

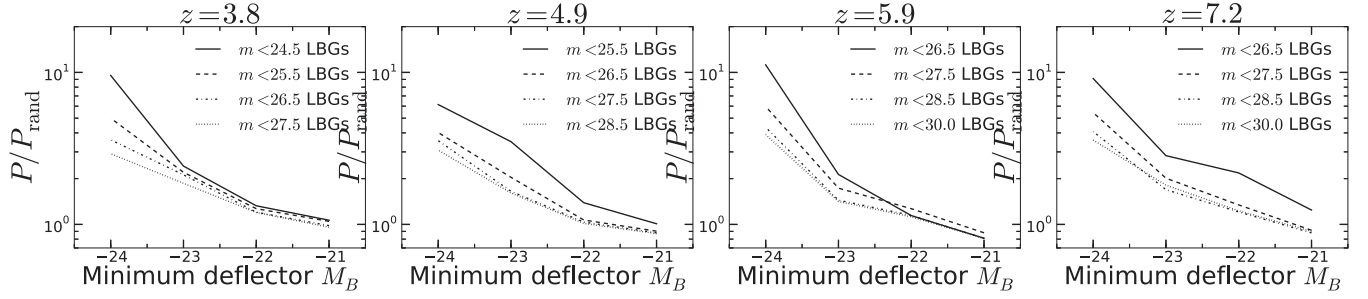


Figure A1. The excess probability of finding an LBG brighter than various flux limits within 5.0 arcsec of defectors brighter than M_B at $z < 2$. In each of the four samples, we find that there is an excess of LBGs around bright foreground objects. The excess becomes monotonically more pronounced with brighter flux limits around bright foregrounds in each of the four samples. At each redshift slice, we consider a different set of flux limits as M_* appears brighter for the lower redshift samples. The right-hand panel shows a large excess of bright LBGs at $z \sim 7$ around bright foreground objects. At $z \sim 4$, we find similar behaviour of bright LBGs appearing more frequently around bright foreground objects than in the total field, but the amplitude of the excess is much lower for the same flux limits of LBGs. However, for brighter flux limits, we see identical behaviour to that observed at higher redshift.

The clustering of bright LBGs nearby massive foreground galaxies is difficult to explain in the absence of magnification bias. One mechanism that could produce such a signal is the enhancement of LBGs around bright, red foregrounds. As discussed in Section 6.3, we searched for this effect in LBG samples with spectroscopic follow-up from the literature, and found no evidence that bright, red foregrounds enhance LBG detection. Therefore, we conclude

that the proximity effect shown in Fig. A1 is consistent with being due to gravitational magnification of background LBGs by massive, bright foreground objects.

This paper has been typeset from a $\text{\TeX}/\text{\LaTeX}$ file prepared by the author.